Journal of Materials Chemistry A

PAPER

View Article Online
View Journal | View Issue

Cite this: J. Mater. Chem. A, 2016, 4, 13488

A study on utilizing different metals as the back contact of $CH_3NH_3PbI_3$ perovskite solar cells†

F. Behrouznejad,[a] S. Shahbazi,[b] N. Taghavinia,*[ac] Hui-Ping Wu[d] and Eric Wei-Guang Diau*[d]

Received 14th July 2016
Accepted 25th July 2016

DOI: 10.1039/c6ta05938d

www.rsc.org/MaterialsA

Organic–inorganic halide perovskite solar cells have attracted considerable interest due to their high efficiency and low fabrication cost. Au and Ag are usually used as the back contact metals but have limitations such as Au is too expensive and Ag is unstable. Here, Pt, Au, Ni, Cu, Cr and Ag were studied as the back contact electrodes for perovskite solar cells. We looked at how the work function of metals can affect their photovoltaic characteristics. The compositional and electrical characterizations were studied using X-ray photoelectron spectroscopy (XPS) and electrochemical impedance spectroscopy (EIS). The general trend observed was that the shunt resistance and open-circuit voltage of the devices decrease with the decreasing work function of the contact metal. The EIS measurements indicated that the internal resistance of the cell decreases when using spiro-OMeTAD in Au, Ag and Pt devices, whereas in the case of Ni, Cu and Cr devices, the internal resistance of the interface increases, indicating that spiro-OMeTAD is not a good HTM with these metal electrodes. Our results also showed that Cu and Ag were not stable in these devices and that the performance of the Ag device degraded faster than that of the Cu device. Efficiencies of 16.4%, 16.5%, 14.7%, 7.8%, 9.2% and 0.04% were obtained for the devices with Au, Ag, Pt, Ni, Cu and Cr, respectively.

Introduction

Organic–inorganic halide perovskite solar cells (PSCs) have attracted wide interest in the fields of solar cells[1–6] and light-emitting diodes (LED),[7,8] due to the intrinsic characteristics of perovskites with a high absorption coefficient (hence high light harvesting ability),[9] good charge carrier mobility[10] (*i.e.* 20 $cm^2 V^{-1} s^{-1}$),[11] large electron and hole diffusion length[12–14] and career lifetime.[15] The perovskite absorber layer is usually formulated as the Pb or Sn compounds $CH_3NH_3Pb(Sn)X_3$, where X can be I,[16,17] Cl,[18] Br[19–21] or a combination of them,[22–25] and the corresponding devices can be fabricated in different architectures, such as planar hetero-junction (PHJ), sensitized or mesoscopic hetero-junction (MHJ). Different formulations provide a tuneable bandgap for colourful solar cells[26] or various coloured LEDs.

PSCs can be fabricated easily by solution-based methods[27–31] with a high crystalline quality that results in highly efficient solar cells that can attain a power conversion efficiency (PCE) of 21.1% (ref. 32) up to 22.1% (confirmed by NREL). Low-temperature preparation methods[27,33–35] have been reported for the PHJ devices[36] with a feasibility for making flexible solar cells.[37–40] However, the high price of Au as a back contact and also spiro-OMeTAD as an organic hole-transporting material (HTM) is a barrier to the commercialization of PSCs.

There are reports on the instability of spiro-OMeTAD due to the formation of voids.[41] An alternative option is to omit the HTM and to use a Au/perovskite structure, but this approach gives inferior efficiencies.[42,43] Replacing an organic hole-transporter by inorganic materials, such as NiO_x (ref. 2 and 44) or NiO,[45–49] copper-doped NiO,[50] CuI, CuSCN[48,51] or Cs_2SnI_6, may improve the long-term stability. Similarly, in planar inverse structures, TiO_2 nanoparticles or nanotubes[52] or ZnO[2,53] can be used to replace the organic electron-transporting material.

Au is conventionally used as the metal back contact. There have been efforts to replace Au with low-cost carbon contacts, in HTM-free[54–57] PSCs or PSCs with NiO nanoparticles[45,46] and nanosheets[58] as the HTM. Recently, efficiencies of about 14.9% and 15% have been reported using ZrO_2/NiO/carbon[45] and Al_2O_3/NiO/carbon[46] structures; however, the efficiency is still inferior to solar cells with a Au/spiro-OMeTAD structure.[59] Another problem with this structure is that normally the carbon composite layer with a porous structure cannot be flexible.

[a]Institute for Nanoscience and Nanotechnology, Sharif University of Technology, Tehran 14588, Iran. E-mail: taghavinia@sharif.edu; Fax: +98-21-66022711; Tel: +98-21-6616 4532

[b]Department of Chemistry, Iran University of Science and Technology, Tehran 1684613114, Iran

[c]Department of Physics, Sharif University of Technology, Tehran 14588, Iran

[d]Department of Applied Chemistry and Institute of Molecular Science, National Chiao Tung University, Hsinchu 30010, Taiwan. E-mail: diau@mail.nctu.edu.tw; Fax: +886-3-5723764; Tel: +886-3-5131524

† Electronic supplementary information (ESI) available: Details of photovoltaic properties and images of device. Details of fitting results of Nyquist plots and also bode plots are also reported. See DOI: 10.1039/c6ta05938d

Other metals that are normally used in optoelectronic devices are Pt, Ag, Ni, Cr and Cu. The prices of Pt, Ag, Ni, Cr and Cu in 2015 were 85.77, 1.36, 0.0278, 0.0057 and 0.0014% of the price of Au (estimations are based on Quandl Financial and Economic Data).

Another important factor in selecting the metal is the chemical and photochemical stability. Ag is the second-most used metal in PSCs.[35,60–64] Ag metal is used in the form of a thin layer,[35,64,65] embedded mesh in the PET substrate covered by a conductive polymer[63] and in an alloy form as a substrate for HTL or ETL. There are some reports[66] and studies[41,67] on the degradation of Ag back contacts in PSCs. Recently, Kato *et al.* showed that AgI can be produced by the reaction of Ag with iodide ions that meet the Ag atoms by migration through the hole-transporting layer.[67]

In the case of Au, nanoporous Au is also used as a substrate for HTL,[68] while Mo[69] and Ni[44,70,71] are also used as sub-layers for HTL, while Al and Cu are used as sub-layers for ETL. Ni is utilized in the form of a thin film as a sub-layer for spiro-OMeTAD[70] and NiO,[44] and in form of a mesh embedded in PET as a substrate for spiro-OMeTAD.[71] Efficiencies of 10.4%, 7.28% and 13.3% have been reported for these structures, respectively. A comparison between the efficiencies of fabricated devices using different metals is reported in Tables S1 and S2.†

In the present research, we examined different metals with relatively high work functions as replacements for Au in Au/HTM/perovskite/ETL/FTO structures. Cu, Ni, Cr, Pt and Au were studied as the usual metals with relatively high work functions and were compared to Ag, which is a relatively low work-function metal. Devices were prepared with and without spiro-OMeTAD to investigate how the work function of metals affect recombination at the interface of the back contact with the perovskite layer, or at the interface of the back contact and the HTM layer. We investigated how these interfacial phenomena affect the shunt resistance, internal resistance and finally open-circuit voltage and the efficiency of the cell. The interfacial resistance and capacitance assessments were done using electrochemical impedance spectroscopy (EIS). The metal surface was studied using X-ray photoelectron spectroscopy (XPS).

Results and discussion

Band alignment and effect on the photovoltaic characteristics

The structure of the PSC as viewed in the SEM cross-section is shown in Fig. 1. It consists of about 200 nm TiO_2 (compact + mesoporous) over an FTO film, followed by a 300 nm perovskite over-layer, 250 nm spiro-OMeTAD (HTM) and about 200 nm metal contact. To study the role of different metal contacts, PSCs without an HTM layer were also fabricated. In HTM-free PSCs, it was expected that metals with different work functions would create more pronounced differences in the cell performance.

The current density *versus* voltage under one sun irradiation for the PSCs, without and with an HTM layer, is shown in Fig. 2a and b, respectively. For the HTM-free PSCs, the performance is largely dependent on the type of metal contact. Generally, Pt and Au contacts lead to larger values of open-circuit voltage (V_{oc})

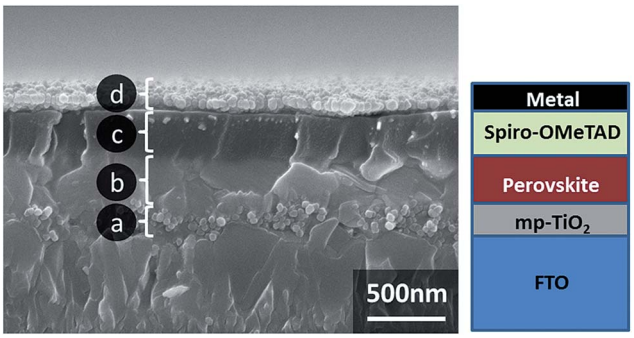

Fig. 1 Cross-sectional SEM image of PSCs: (a) mesoporous TiO_2 layer deposited on the TiO_2 compact layer, and filled by $CH_3NH_3PbI_3$, (b) perovskite over-layer, (c) spiro-OMeTAD thin film and (d) back contact metal (here Ag). For some of the PSCs in this paper.

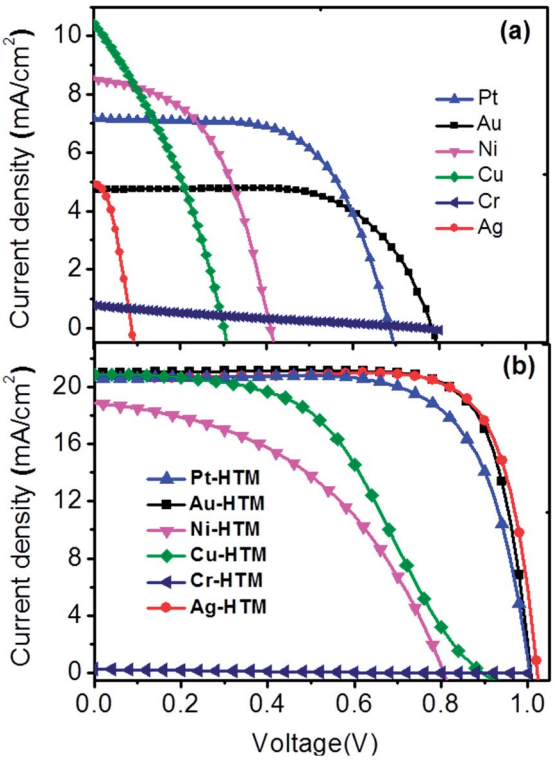

Fig. 2 Current-density–voltage curves of (a) HTM-free PSCs and (b) PSCs with a spiro-OMeTAD HTM layer. For the HTM-free devices, the current density is lower and the device performance is apparently dependent on the metal contact. The addition of spiro-OMeTAD weakens the effect of the metal contact, while improving the current density and voltage. "Sp" represents spiro-OMeTAD.

and lower values of short-circuit current density (J_{sc}). In contrast, Ni and Cu contacts result in larger J_{sc} and lower V_{oc}. There is an anomaly for the cases of Cr and Ag; whereby the Cr PSC shows a high V_{oc} and very low J_{sc} and the Ag PSC shows a very low V_{oc} and higher J_{sc}. The impact of the metal contact is more negligible for PSCs with an HTM layer (Fig. 2b). The J_{sc} values are considerably larger than those of HTM-free PSCs, and they also show better V_{oc} values. Pt, Au and Ag show the best

Table 1 Photovoltaic characteristics of HTM-free PSCs and PSCs containing HTM (spiro-OMeTAD)

Sample	J_{sc} (mA cm^{-2})	V_{oc} (V)	FF	PCE_{max} (%)	PCE_{AVG} (%)	S (%)
Au	4.85	0.809	65.38	2.56	2.46	0.08
Ag	4.93	0.087	39.34	0.17	0.11	0.07
Pt	7.17	0.686	62.6	3.08	2.92	0.25
Ni	8.52	0.411	49.92	1.75	1.46	0.27
Cu	10.42	0.301	33.69	1.06	0.55	0.33
Cr	0.89	0.753	21.83	0.14	0.12	0.015
Au-HTM	20.99	1.0091	77.60	16.44	16.40	0.06
Ag-HTM	20.60	1.023	78.32	16.51	16.25	0.23
Pt-HTM	20.58	1.006	71.07	14.72	14.51	0.19
Ni-HTM	18.21	0.834	51.61	7.83	7.30	0.47
Cu-HTM	20.32	0.942	47.89	9.17	8.79	0.27
Cr-HTM	0.47	0.04	18.41	0.04	0.05	0.006

device performance. The Cr contact again shows a low current density. Table 1 displays a summary of the device performances for PSCs with and without HTM and having different metal contacts. We focus herein on the case of HTM-free PSCs to study how metal contacts with different work functions affect the band bending and carrier collection.

Fig. 3a illustrates how V_{oc} and R_p (shunt resistance) of the cells vary with the type of different metal contact electrodes. The metals are ordered based on their work function values. There is a trend on V_{oc}, whereby it decreases as the metal work function is decreased. The clear exception to this trend is Cr, which shows a good V_{oc}, while its work function is not as high. This might be due to the formation of a native chromium oxide blocking layer on the electrode surface.

For R_p also, a similar trend can be noted. In terms of both V_{oc} and R_p, Au shows higher values compared to Pt, while Pt has a higher work function than Au.

Fig. 3b illustrates the energy level alignment of the layers and demonstrates the role of the metal work function. Photo-generated electrons and holes created in the conduction band (−3.91 eV) and the valence band of $CH_3NH_3PbI_3$ (−5.43 eV)[72] can be expected to be captured by TiO_2 and the metal, respectively. TiO_2 with a conduction band energy of about −4.0 eV has been shown to be an ideal electron selective material in PSCs.[73] It has a deep valence band energy of about −7.3 eV, making it a good hole-blocking layer. Photo-generated holes are expected to be captured by the back contact. In the case of using HTM (spiro-OMeTAD), the holes are collected by the HOMO level of HTM; hence, a deeper HOMO results in larger V_{oc}.[21] In practice, the HTM layer has also the function of preventing a short circuit in the device by producing a compact capping layer between the metal electrode and the perovskite layer.[74] Spiro-OMeTAD acts also as an electron-blocking layer, resulting in increasing V_{oc}.

For the HTM-free case of Fig. 3b, the metals (Ag, Cr, Cu, Ni, Au, Pt with work functions of 4.26 eV, 4.5 eV, 4.65 eV, 5.15 eV, 5.1 eV and 5.65 eV (ref. 75)) act as the back contact electrodes. Here, while the work functions are different, the metals can theoretically capture both electrons and holes, leading to a low V_{oc} and sloped J–V curves at the short-circuit point (*i.e.* a low shunt resistance[76]), as indicated in Fig. 3a. However, the difference in the performance of the PSCs with different metals is explained by the band bending created at the interface of the metal and perovskite. This is illustrated in Fig. 3c–g.

The band bending nature at the interface of $CH_3NH_3PbI_3$ and the metal is dependent on the relative position of the Fermi level for the metal and perovskite. The positions of the conduction and valence bands of $CH_3NH_3PbI_3$ have been reported in many articles,[77,78] but the reported position of the Fermi level is different in the different research studies.[79] Also, there are some reports that introduce $CH_3NH_3PbI_3$ as an n-type semiconductor.

X. Liu *et al.*[74] showed that $CH_3NH_3PbI_3$ deposited on the ITO/PEDOT substrate shows n-type semiconducting properties with a bandgap of 1.7 eV (with a valence band energy about −1.0 eV lower than the Fermi level).

It has been shown that after Au deposition on $CH_3NH_3PbI_3$ film, the energy offset between the valence band edge of $CH_3NH_3PbI_3$ and the Fermi level of the system is 0.6 eV, which results in low energy loss during a hole transferring to the Au back contact. Also, there are some reports that introduce $CH_3NH_3PbI_3$ as a p-type semiconductor.[55,73,80–82] Laban *et al.* reported an HTM-free p-type PSC with a Au back contact with 8% efficiency.[80]

W. Yin *et al.*[83] exhibited that there are p-type vacancies related to Pb and also n-type vacancies related to $CH_3NH_3^+$, which produce the shallow levels responsible for the semiconductor type (p or n). While the work function of the perovskite layer is known to be dependent on the preparation method,[79] surface contamination and the method of measurement, Miller *et al.* indicated that it also greatly dependent on the substrate material on to which $CH_3NH_3PbI_3$ is deposited. It is reported that, dependent on the kind of substrate (p-type or n-type), the value of $E_f - E_v$ can be changed, and that its value is larger when it is deposited on an n-type substrate. It has been shown that the work function can change from 3.72 eV in the case of $CH_3NH_3PbI_3$ deposited on FTO/TiO_2/Al_2O_3 to 5.01 eV in the case of $CH_3NH_3PbI_3$ deposited on ITO/PEDOT:PSS.[79] We can thus conclude that the charge carrier density in the $CH_3NH_3PbI_3$ layer is low and under the influence of the carrier density of its under-layer, whereby the work function changes significantly. This implies that $CH_3NH_3PbI_3$ practically acts like an intrinsic semiconductor, so it is reasonable to assume its Fermi level is at the middle of the bandgap, at around −4.65 eV.

Although the fabrication procedure determines the extent and type of the Frenkel defects[15,83] and, therefore, the type of perovskite layer, it is indicated that the main defects in $CH_3NH_3PbI_3$ are of a Schottky type, where the overall stoichiometry does not change; therefore, assuming that $CH_3NH_3PbI_3$ is an intrinsic semiconductor is reasonable[84,85] The band bending diagrams calculated by SCAPS software in the dark condition are shown in Fig. 3c–g for HTM-free devices with different metals as the back electrode. The Fermi level was assumed to be around −4.65 eV for the calculations. Other reported values for the Fermi level of $CH_3NH_3PbI_3$ in the literature lie in the range of 0.5 eV higher or lower than this value.[74,79,86,87] The calculated energy–band diagrams for Fermi levels 0.5 eV above or below

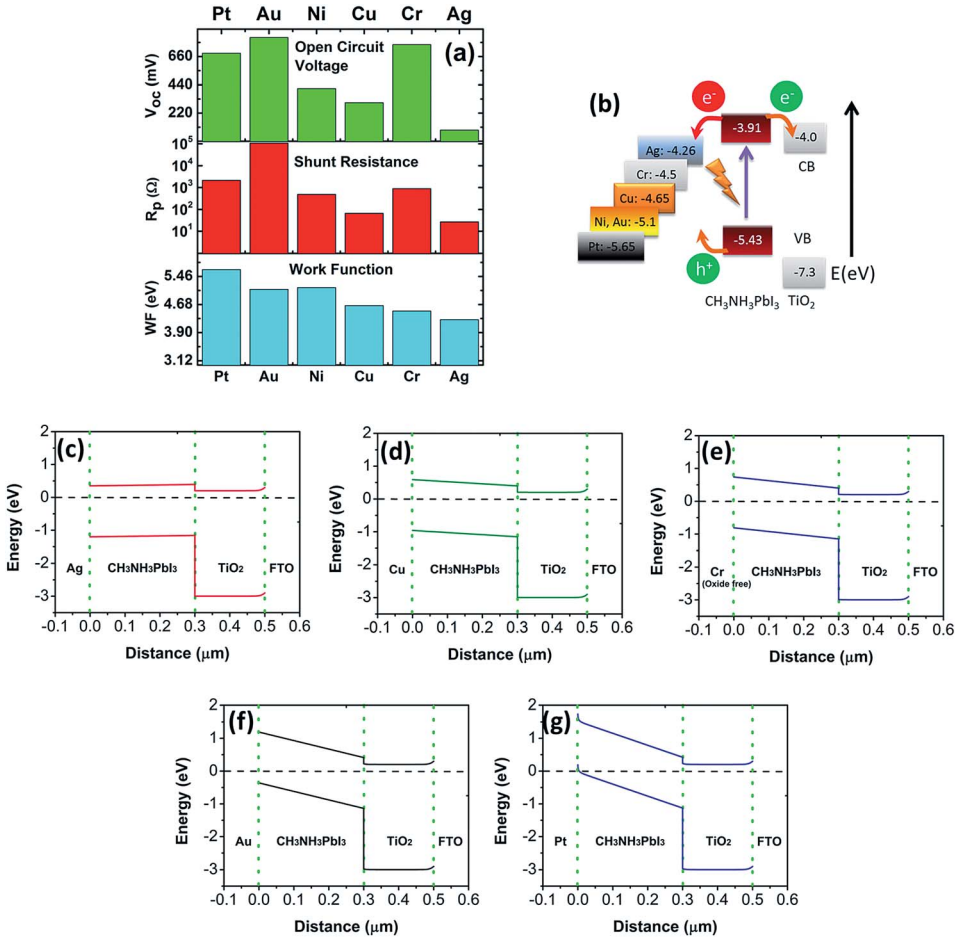

Fig. 3 (a) Open-circuit voltage and shunt resistance of HTM-free PSCs with Pt, Au, Ni, Cu, Cr and Ag as back contact metals. The work function of metals are also shown. (b) Energy level alignments: TiO_2 electron selective layer and $CH_3NH_3PbI_3$ perovskite absorber against the Fermi level of different contact metals. (c to g) Energy diagram of FTO/TiO_2/$CH_3NH_3PbI_3$/metal structure with different metals as the back electrode (simulated by SCAPS software in the dark condition). In the case of Ag, there is a Schottky barrier against electron transfer from $CH_3NH_3PbI_3$ to the metal and electrons can transfer from this material to Ag. By increasing the metal work-function from Cu to Pt, the Schottky barrier against electrons transferring from $CH_3NH_3PbI_3$ increases significantly but holes transfer is easier.

the mid-gap value do not change significantly compared to the initial diagram (Fig. S1 to S5†). Due to the low effective mass of electrons and holes in the $CH_3NH_3PbI_3$ lattice (about $0.15m_0$ for electrons and $0.18m_0$ for holes[88]), the effective density of states is very small and, therefore, the carrier concentration is not high in these perovskite materials. This demonstrates that the type of isolated $CH_3NH_3PbI_3$ as a semiconductor and the value of its work function make no remarkable contribution in the electrical performance of the PSC device. In the case of low work-function metals, electrons transfer from the Fermi level of the metal into the conduction band of the perovskite. The polarized interface results in a Schottky barrier against hole transfer from the valence band of perovskite to the metal (Fig. 3c), while the electrons can easily transfer from the conduction band of perovskite to the metal. This results in low R_p and V_{oc}, which is consistent with our experimental results.

R_p for Ag and Cu devices are almost the same and have the lowest value among all the metals due to the easy recombination of photo-electrons through the metal interface. In the case of Cr, the first layer during vacuum deposition at about 2×10^{-5} Torr is an oxide layer. This oxide layer acts as a barrier layer,[89,90] therefore V_{oc} is higher due to this barrier layer compared to other HTM-free PSCs. This barrier layer also leads to a decreased current density (Fig. 2). We already reported this effect in dye-sensitized solar cells when the Cr substrate was used as a substrate for a photoanode[89,91] and counter electrode.[90,91]

In the case of noble metals (Pt and Au), there is no oxide layer or interfacial chemical reaction between these metals and the perovskite layer, hence the work function is expected to be the most influential parameter. In these cases with work functions higher than that of perovskite, an inverse bending direction is realized, where photo-generated holes can easily transfer to the metal, while there is a Schottky barrier towards the electron transfer. This barrier is highest in the case of Pt and Au due to their high work functions (Fig. 3e and f), and therefore, they show a higher V_{oc} than the other metals. In the case of Cr, a compact native oxide layer is known to form, therefore the

influence of the work function is not clearly realized, as shown in Fig. 3a. The work function of Ni is relatively high. The open-circuit voltage of Ni is higher than that of Cu and Cr but lower than that of Au. Ni, with a work function of about −5.15 eV, is expected to produce similar results as Au, but in practice it shows inferior performance. This inferior performance was also reported by Q. Jiang *et al.*, who confirmed our results. They reported an FF of 0.61 and 0.67 in the case of PSCs with Ni and Au (with almost the same metal thin film resistance), respectively.[70] The work function reported for Ni is more than 5.0 eV, but this value is related to the single crystal structure of Ni, and its value for a thin film structure that is deposited on a rough surface is different, while in the case of a rough surface, the work function of Ni can be as low as 4.44 eV. In addition, a NiO_x layer may form during the deposition and this layer can also affect the interface and the band bending. In addition to work function and interface chemistry; the film uniformity is also an important factor and Ni usually shows inferior properties in this respect. The major parameter is ductility, or the ability of the metal to deform under tensile stress. The optical images show that the Ni layer that is deposited on the $CH_3NH_3PbI_3$ layer is a crackless layer, while one day after the deposition of Ni on the spiro-OMeTAD layer, a non-uniformity of the Ni layer is distinguishable from the backside of PSC (Fig. S10d in comparison with Fig. S10c†). The ductility of Au, Pt, Ag, Cu, Ni, and Cr is 0.93, 0.76, 0.73, 0.62, 0.5 and 0.18 respectively. This low ductility of Ni may result in disintegration of the film under mismatch stress caused by the under-layer or under thermal stress, and will confine the deposition conditions and type of under-layer. The mentioned phenomena in the above paragraphs may explain the higher series resistance (lower FF) of PSCs with Ni as the cathode compared to PSC with Au as the cathode.

The lowest work functions among these metals are related to Ag and Cu. Duo to their low work function, holes cannot transfer to the metal substrate efficiently (Fig. 3c and d), but electrons can transfer from the metal to the perovskite layer and decrease the open-circuit voltage, as indicated in Fig. 2 and 3a.

The internal resistances of the devices were investigated using EIS (Fig. 4). The charge separation phenomena due to dipoles at the interfaces could be modelled as constant phase elements parallel with the charge transfer resistance. The built-in potential (the difference between the work functions of adjacent materials) is responsible for the interfacial capacitance. The first semi-circle in the high-frequency region (10^4 to 10^6 Hz) is attributed to charge transfer at the interface of the back contact electrode.[45,58] The second semi-circle (in an intermediate frequency region) is related to the recombination phenomena[92] at the interface of $CH_3NH_3PbI_3$ and the TiO_2 or HTM layer. The third region, with frequencies lower than 1 Hz, is attributed to ion diffusion and hysteresis or dielectric relaxation processes[93] (low-speed phenomena), but this is not investigated in this article. For Ag devices, it is clear that R_{ct} at the interface of the metal and HTM is significantly lower than that of the HTM-free device (Fig. 4). The internal resistance in the case that there is no HTM, for Pt, Au and Ag, is significantly lower than for Ni, while Ni is lower than Cu and Cr. In the case of Cr, it seems that the interfacial oxide layer greatly increases the total internal resistance, while deposition at a lower pressure may damage the spiro-OMeTAD layer. By utilizing the HTM layer, the total internal resistance of the PSCs is decreased significantly for Ag, Au and Pt, while it is increased for Ni, Cu and Cr. This confirms that the interfacial resistances at the interface of spiro-OMeTAD (with valence energy level of −5.1 eV [94]) and the metal electrodes are high and forms a non-ohmic contact with Cu or Ni. Jeong *et al.* utilized Mo with a work function of 4.6 eV as the cathode in PSCs with the structure of FTO/TiO_2/$CH_3NH_3PbI_3$/spiro-OMeTAD. They showed that by increasing the time of sputtering and increasing the thickness of the Mo layer from 80 nm to 140 nm, the fill factor decreases from 67.77 to 57.03 due to penetration of the Mo atoms through the spiro-OMeTAD layer and produces a non-ohmic contact with $CH_3NH_3PbI_3$ that results in increasing series resistance and an S-shape *I–V* curve.[69] Copper also has the same work function, and we can see the S-shape *I–V* curve in our results in Fig. 2b. We can attribute this phenomenon to the penetration of Cu atoms through the HTM. We can thus conclude that spiro-OMeTAD is not a good HTM for Cu and Ni. The large internal resistance results in sloped *J–V* curves at the V_{oc} point, thus leading to a low fill factor (Fig. 2).

The CPE of the Cu–$CH_3NH_3PbI_3$ interface is higher than that of Ni–$CH_3NH_3PbI_3$, while that of Pt–$CH_3NH_3PbI_3$ is higher than that of Au–$CH_3NH_3PbI_3$. This is due to the higher built-in potential (the difference between the work functions of adjacent materials, V_{bi}). There is an anomaly for Ag/$CH_3NH_3PbI_3$, in that its V_{bi} is the highest among all the HTM-free devices (except Cr/CrO_x), but its capacitance is low. As discussed in the following paragraphs, AgI is produced rapidly at the interface of Ag and $CH_3NH_3PbI_3$ (silver colour is clearly distinguishable from the backside of PSC) and this changes the interfacial CPE.

Chemical stability of the metal contacts

An investigation of the photochemical reactions at the interface of the metal and the perovskite material (here $CH_3NH_3PbI_3$) and at the interface of the metal and the hole-transport material (here spiro-OMeTAD) is necessary for selecting the appropriate contact metals.

The formation of unwanted phases at the interface of the metal and HTM, or at the interface of the metal and $CH_3NH_3PbI_3$, can increase the internal resistance of the cell by producing a non-ohmic contact.

It has also been shown that the parts under illumination corrode faster.[41] For the Ag interface with $CH_3NH_3PbI_3$, corrosion phenomena have already been reported.[41,67] In the case of HTM-based devices, the colour of Ag changes to yellow due to AgI formation, but when there is no HTM, the colour changes to grey again due to the photosensitization and decomposition of AgI (Fig. S6†). This indicates that the HTM layer protects Ag against light-induced corrosion to some extent and decreases the rate of reaction. This degradation can occur by the reaction of Ag and the migrated I^- ions directly or by using degraded $CH_3NH_3PbI_3$. The proposed degradation equation for the perovskite is:[6,41]

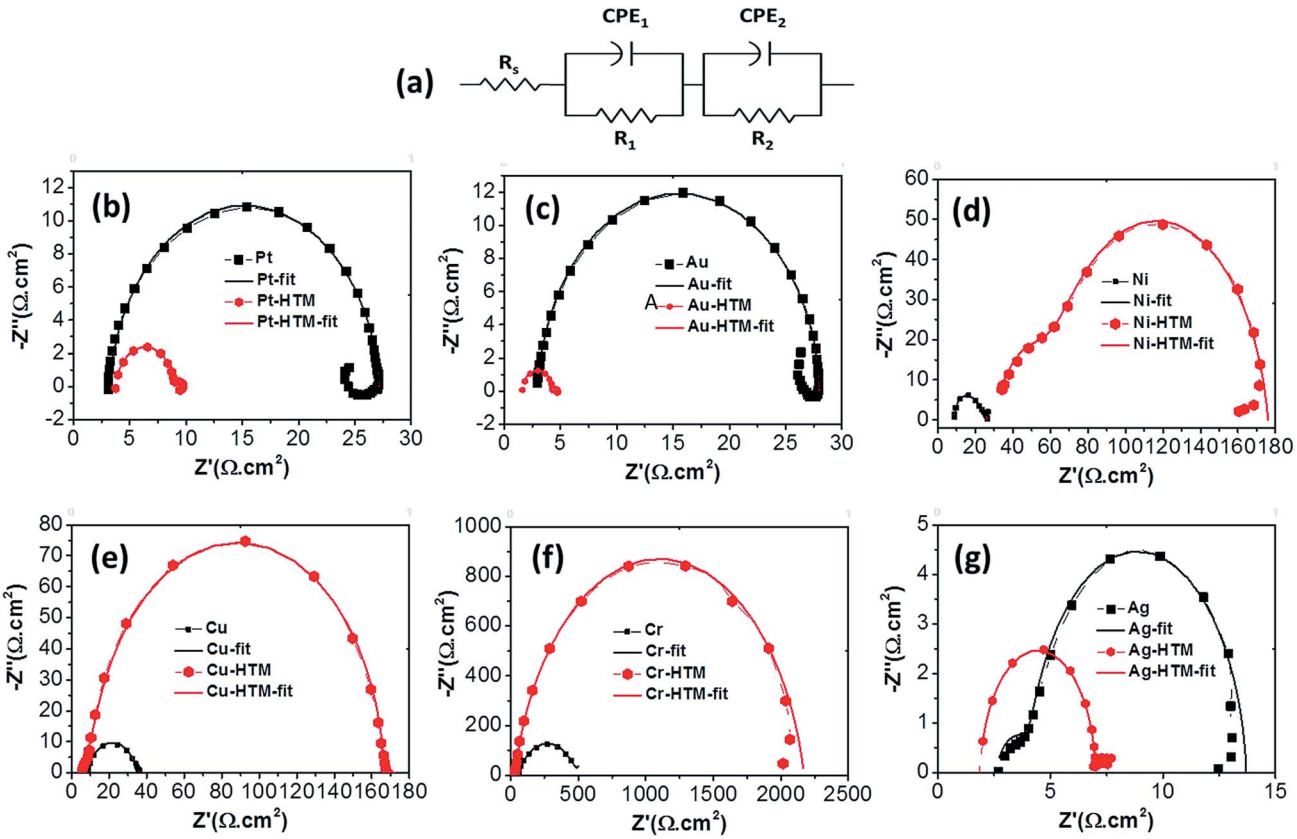

Fig. 4 Equivalent circuit and Nyquist plots for HTM-free PSCs with Pt, Au, Ni, Cu, Cr and Ag as a back contact electrode in comparison with PSCs utilizing spiro-OMeTAD as the HTM. HTM represents spiro-OMeTAD (frequency range is from 1 Hz to 1 MHz).

$$H_2O + [(CH_3NH_3^+)PbI_3]_n \rightarrow [(CH_3NH_3^+)_{n-1}(CH_3NH_2)_nPbI_3][H_3O] \rightarrow HI + CH_3NH_2 + PbI_2 + H_2O + [(CH_3NH_3^+)PbI_3]_{n-1} \quad (1)$$

In the presence of sufficient water molecules, $CH_3NH_3PbI_3$ can degrade completely to PbI_2. In this reaction, HI is produced and may react with the metal, in particular Ag. Ion migration in the perovskite layer is also important in initiating degradation. C. Eames *et al.* reported that the activation energy for the migration of I^-, MA^+ and Pb^{2+} vacancies are 0.58 eV, 0.84 eV and 2.31 eV, respectively.[95] Therefore, I^- migration is more feasible than the other ions. It is claimed that in the presence of a photovoltage or an externally biased voltage, negative ions can diffuse to the electron-transport layer while positive ions can diffuse to the hole-transport layer, but in the absence of an electric field, ions diffuse randomly.[96] A lower activation energy of 0.08 eV was calculated by Azpiroz *et al.* for iodine vacancies.[96] Based on this calculation, the thermal fluctuations can overcome the activation energy of I^- and these ions can diffuse randomly and may cause corrosion on the metal surface. There are also reports on the presence of CH_3NH_3I on the surface of Ag, detected using XPS.[67]

Fig. 5 displays the XPS spectra for Ag and Cu deposited directly on the $CH_3NH_3PbI_3$ layer. The measurements were performed three months after fabrication, in order that the migrations and reactions would have had sufficient time to take effect. The Shirley method was used for background subtraction. Fig. 5a indicates that the metallic $Ag_{5/2}$ and $Ag_{3/2}$ peaks shift to lower energies, which is attributed to the formation of AgI. Fig. S6† exhibits the backside and front-side image of PSCs with Ag as the back contact metal. It is indicated that AgI formation does not protect Ag from further corrosion, and that corrosion leads to the disappearance of some parts of the Ag layer. AgI is known to readily form at room temperature and is again reduced to Ag under illumination. Silver halides are used in photography films due to this photochromic effect. In photography films, a dye is used for light absorption and electron injection into the conduction band of silver halide. Here, AgI is formed on the backside of $CH_3NH_3PbI_3$. The conduction band energy of AgI is about −4.0 eV,[97] while that of $CH_3NH_3PbI_3$ is about −3.91 eV. It seems that photo-generated electrons in the conduction band of $CH_3NH_3PbI_3$ can transfer to the conduction band of AgI. The scenario that is explained for silver halides in photography film is that silver ions in grain boundaries can trap one electron to form a silver atom. The Ag atom has a high electron affinity of about 1.3 eV, and so can trap a second electron to form Ag^-. Ag^- with Ag^+ can react as in eqn (2):[98]

$$Ag^- + Ag^+ \rightarrow Ag_2 \quad (2)$$

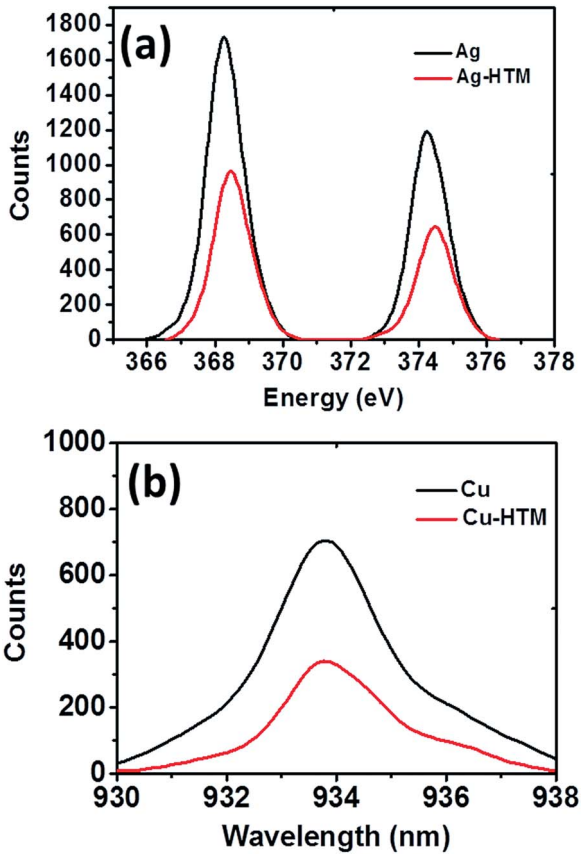

Fig. 5 XPS spectra of Ag (a) and Cu (b) deposited directly on the $CH_3NH_3PbI_3$ (black line) and on the HTM layer (red line). The experiment was done three months after deposition. The higher energy peaks in the case of Ag and the peak shoulder in the case of Ag and the peak shoulder in the case of Cu are due to the presence of metallic Ag and Cu materials. These peaks shifts to the lower energies in the case of Ag and the shoulder disappears in the case of Cu, due to the faster chemical reaction of Ag and Cu with iodine in HTM-free devices.

Ag_2 can trap electrons and react with Ag^+ again to form a larger cluster. Hence, one cannot expect to have a uniform AgI layer, due to this decomposition process. Therefore, further iodine and other ions can diffuse through this layer to react with the Ag layer and produce AgI. This effect results in the fast degradation of both the $CH_3NH_3PbI_3$ and Ag layer (Fig. S6†). In the case of PSCs with an HTM layer, electron injection into the AgI layer is inhibited. The Fermi level of spiro-OMeTAD is about −5.1 eV, and it acts as an electron-barrier layer. The bright yellow colour of AgI is distinguishable in Fig. S6d & f.† The diffusion process is also slower due to the low speed of diffusion.

In the case of Cu (Fig. 5b), the shoulder at higher energy is related to the metallic binding energy, which disappears in the case of HTM-free devices due to fast degradation. For the other metals, namely Au, Pt, Ni and Cr, the colour of $CH_3NH_3PbI_3$ does not change significantly, as shown in Fig. S9–S12.† Although Cu [$3d^{10}4s^1$], Ag[$4d^{10}5s^1$] and Au[$5d^{10}6s^1$] are in the same group in the periodic table, their chemical stabilities are completely different due to relativistic effects. The relativistic effect results in d-orbital expansion and s-orbital contraction.[99,100]

This effect is significant in Au due to its heavier nucleus and results in a lowering of the energy of the 6s orbital by approximately 1.63 eV.[101] The first ionization potential of Au due to this effect is 9.2 eV, which is significantly higher than that of Cu and Ag, which are 7.7 eV and 7.6 eV, respectively, and this is the cause of its high chemical resistance.[102] The relativistic effect in the case of Pt[$5d^9 4s^1$] is also considerable; its ionization potential is 9.0 eV,[103] while that of Ni as its cohort is 7.6 eV. The relativistic effect in Pt is slightly weaker than in Au (the fractional contraction of the 6s shell for Pt is 0.838, while that for Au is 0.828 (ref. 104)), but is stronger than in other metals, so it also has a good chemical stability.

Optical effects of the metal contacts

Here in this section, we briefly investigate whether the metal contacts of different types have any optical effects. In dye-sensitized solar cells (DSC), there is always a back-reflecting layer that reflects the unabsorbed light back into the cell and improves the quantum efficiency. In solid-state DSCs, the metal contact serves also as the back-reflecting layer and shows an important optical effect. The question is whether the metal contacts in PSCs contribute to light management in the device.

The optical reflectivity of the metals is different, as shown in Fig. 6a. Metals were vacuum deposited on glass substrates (Au, Ni, Ag by vacuum evaporation and Cu, Cr, Pt by DC magnetron sputtering). The highest reflectivity belonged to Ag, which was close to 100%. For Au and Cu, there was an absorption edge at around 530 nm and 570 nm, below which the reflectivity fell to about 40%. For Pt, Ni and Cr, typical reflectivity values were around 70%, 50% and 40%, respectively. The 5d to Fermi level transition energy for Au metal is about 2.3 eV, so it absorbs blue and green part of the visible spectrum and looks golden. The light absorption of Ag is 3.5 eV (in UV), so it reflects in the visible spectrum.[104] The reddish colour of Cu is due to the 3d–4s transition energy, which is about 1.8–2.0 eV, so it also absorbs yellow and looks red.

Fig. 6b shows the IPCE of devices with and without an HTM layer, with different metals as the back contact. The thickness of the $CH_3NH_3PbI_3$ layer is similar in all the PSCs, so the light harvesting is almost the same for all PSCs. Despite the remarkable difference in the reflectivity of the metals, the IPCE values are almost independent of the type of metal back contact. This demonstrates that the perovskite layer is sufficiently thick to absorb almost all the light, and the reflecting property of the metal back contact makes no considerable improvement in light harvesting.

For HTM-free PSCs, a notable decrease in IPCE was observed for the red part of the spectrum. This was related to the wavelength-dependent penetration depth of light. The penetration depth of light for blue is smaller than for red, hence the blue part of light is absorbed near the interface of the TiO_2 electron-transporting layer, where photo-generated electrons are readily captured in TiO_2. In the case of red light, a large part of the photo-generated carriers are produced near the perovskite-metal interface, where recombination through metal contact is very likely.

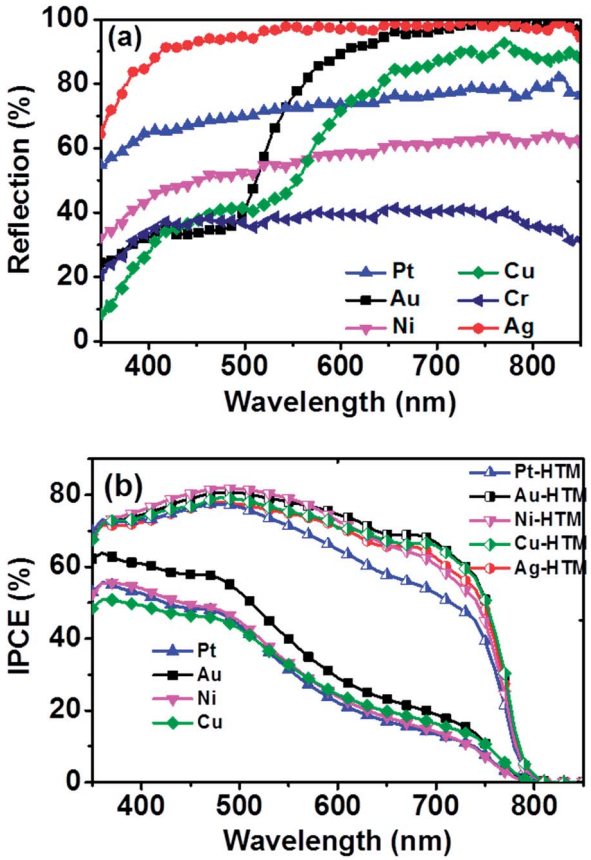

Fig. 6 (a) Diffuse reflectance of Pt, Au, Ni, Cu, Cr and Ag thin films: Au, Ni and Ag were deposited using vacuum evaporation, while Cu, Cr and Pt were deposited using DC magnetron sputtering on glass substrates. (b) IPCE data for HTM-free PSCs compared to PSCs with spiro-OMeTAD HTM: in the case of HTM-free devices, IPCE data are related to devices that have relatively the same current density (Tables S1, S3, S5, S7, S9 and S11†). As shown, the shape of the IPCE curves is independent of the reflection of the metal contact. There is a large loss in the red part of the spectrum of the HTM-free devices.

Experimental

A 50 nm thick layer of TiO_2 was deposited using (titanium(diisopropoxide) bis(2,4-pentanedionate) 75% in isopropanol (Sigma-Aldrich))/EtOH (1 : 15) solution. The layer was deposited by spray pyrolysis at 350 °C followed by sintering at 500 °C for 30 min. A 200 nm thick TiO_2 mesoporous layer was deposited using the spin-coating of diluted TiO_2 paste (20 wt%, Sharif Solar) containing nanoparticles 20 nm in diameter (the paste was diluted with EtOH in a ratio of 1 : 8). The deposited TiO_2 layer was heated at 325 °C (10 min), 375 °C (10 min), 450 °C (15 min) and sintered at 500 °C for 30 min. Further deposition steps were carried out in a N_2-filled glove box to avoid degradation by moisture. A 45 wt% perovskite solution was prepared by dissolving 400 mg CH_3NH_3I and 1156 mg PbI_2 in anhydrous-dimethylformamide (DMF). The solution was stirred for about 12 h at 70 °C and filtered using a 0.45 μm PVDF membrane. The $CH_3NH_3PbI_3$ layer was deposited using a one-step deposition method, by spin-coating 80 μL of prepared solution, followed by spin-casting 0.24 mL chlorobenzene in the 4th second of rotation (at a speed of 5000 rpm). The samples were heated on a hot-plate at a temperature of 100 °C for 10 min. The thickness of the $CH_3NH_3PbI_3$ over-layer was about 300 nm. The spiro-OMeTAD solution was prepared by dissolving 82.6 mg spiro-OMeTAD, 22 μL tertbutylpyridine and 16 μL solution of lithium bis(trifluoromethane-sulfonimide) (with a concentration of 50 mg/100 μL in acetonitrile) in 1 mL chlorobenzene. A 200 nm thick spiro-OMeTAD layer was deposited by spin-coating at 2000 rpm for 30 s. A physical vapour deposition method was used for depositing Au, Ag and Ni, while Pt, Cr and Cu were deposited using a DC magnetron sputtering system with a base pressure of 2×10^{-5} Torr. The Ar pressure was 4×10^{-3} Torr. Current density–voltage measurements were done under AM1.5 conditions using the Solar-simulator (XES-40S1, SAN-E1), a standard silicon reference cell (VLSI Standards, Oriel PN 91150 V) and a Keithly 2400 digital source meter. The incident photon to current conversion efficiency was measured using a Xe lamp (PTiA-1010, 150W), a monochromator (PTi-1200 gr mm^{-1} blazed at 500 nm) and a Keithly 2400 digital source meter. The internal and interfacial resistance in PSCs were measured under an LED light using electrochemical impedance spectroscopy, by an electrochemical system (Zahner). Cross-sectional scanning electron microscopy images were recorded using a Hitachi SU-8010 system. Diffuse reflectance spectra were measured using an Avantes spectrometer. X-ray photoelectron spectroscopy (Specs-EA10+) with an Al X-ray source was used for analysing the surface compositions.

Conclusions

The role of different metals as a back contact electrode on the performance of PSCs was studied. Results show that Au is still the optimum metal for use with spiro-OMeTAD as the back contact, while Pt provides better performance compared to Ag, Cu, Ni and Cr. This is due to the high stability and also high work function of Pt (about 5.65 eV). For HTM-free PSCs, this high work function led to favourable band bending at the perovskite-metal interface, providing a barrier to electron transfer from perovskite to the metal. For PSCs with HTM, Pt formed a low interfacial resistance with the HTM. Efficiencies of 14.3% and 16.4% were obtained for Pt- and Au-based cells with HTM and 3.1% and 2.6% for Pt and Au cells without HTM. Pt and Au were chemically stable, while Cu and Ag were unstable, especially in the HTM-free devices where the former and the later electrodes would form CuI and AgI, respectively. The photodecomposition of AgI in the presence of $CH_3NH_3PbI_3$ provides ways for diffusing iodide ions through the absorber layer, resulting in fast performance degradation of the devices. Ni and Cr were apparently stable but the EIS spectra indicated that spiro-OMeTAD is not a good HTM for use with these metals. The efficiency was inferior due to the formation of a barrier layer at the interface of the metal and HTM, therefore the appropriate HTM with corresponding valence and conduction band energy levels should be chosen. Efficiencies of 16.5%, 7.8%, 9.2% and 0.05% were obtained for devices fabricated with the Ag, Ni, Cu and Cr electrodes with spiro-OMeTAD,

respectively, but corresponding efficiencies of 0.17%, 1.75%, 1.06% and 0.14% were obtained without spiro-OMeTAD.

References

1 W. Zhang, M. Saliba, D. T. Moore, S. K. Pathak, M. T. Horantner, T. Stergiopoulos, S. D. Stranks, G. E. Eperon, J. A. Alexander-Webber, A. Abate, A. Sadhanala, S. Yao, Y. Chen, R. H. Friend, L. A. Estroff, U. Wiesner and H. J. Snaith, *Nat. Commun.*, 2015, **6**, 6142.
2 J. You, L. Meng, T.-B. Song, T.-F. Guo, Y. Michael Yang, W.-H. Chang, Z. Hong, H. Chen, H. Zhou, Q. Chen, Y. Liu, N. De Marco and Y. Michael Yang, *Nat. Nanotechnol.*, 2015, **11**, 78–81.
3 Y. Yang, D. P. Ostrowski, R. M. France, K. Zhu, J. van de Lagemaat, J. M. Luther and M. C. Beard, *Nat. Photonics*, 2015, **10**, 53–59.
4 A. Fakharuddin, F. Di Giacomo, A. L. Palma, F. Matteocci, I. Ahmed, S. Razza, A. D'Epifanio, S. Licoccia, J. Ismail, A. Di Carlo, T. M. Brown and R. Jose, *ACS Nano*, 2015, **9**, 8420–8429.
5 Y. Fang, Q. Dong, Y. Shao, Y. Yuan and J. Huang, *Nat. Photonics*, 2015, **9**, 679–686.
6 J. M. Frost, K. T. Butler, F. Brivio, C. H. Hendon, M. van Schilfgaarde and A. Walsh, *Nano Lett.*, 2014, **14**, 2584–2590.
7 A. B. Wong, M. Lai, S. W. Eaton, Y. Yu, E. Lin, L. Dou, A. Fu and P. Yang, *Nano Lett.*, 2015, **15**, 5519–5524.
8 S. D. Stranks and H. J. Snaith, *Nat. Nanotechnol.*, 2015, **10**, 391–402.
9 M. A. Green, A. Ho-Baillie and H. J. Snaith, *Nat. Photonics*, 2014, **8**, 506–514.
10 H. Oga, A. Saeki, Y. Ogomi, S. Hayase and S. Seki, *J. Am. Chem. Soc.*, 2014, **136**, 13818–13825.
11 T. Eijtens, S. D. Stranks, G. E. Eperon, R. Lindblad, E. M. J. Johansson, J. M. Ball, M. M. Lee, H. J. Snaith, I. J. Mcpherson, T. Leijtens, S. D. Stranks, G. E. Eperon, R. Lindblad, E. M. J. Johansson, I. J. Mcpherson, H. Rensmo, J. M. Ball, M. M. Lee and H. J. Snaith, *ACS Nano*, 2014, **8**, 7147–7155.
12 G. Xing, N. Mathews, S. S. Lim, Y. M. Lam, S. Mhaisalkar and T. C. Sum, *Science*, 2013, **6960**, 498–500.
13 Q. Dong, Y. Fang, Y. Shao, P. Mulligan, J. Qiu, L. Cao and J. Huang, *Science*, 2015, **347**, 967–970.
14 S. Bai, Z. Wu, X. Wu, Y. Jin, N. Zhao, Z. Chen, Q. Mei, X. Wang, Z. Ye, T. Song, R. Liu, S. Lee and B. Sun, *Nano Res.*, 2014, **7**, 1749–1758.
15 J. Kim, S. H. Lee, J. H. Lee and K. H. Hong, *J. Phys. Chem. Lett.*, 2014, **5**, 1312–1317.
16 M. L. Agiorgousis, Y. Sun, H. Zeng and S. Zhang, *J. Am. Chem. Soc.*, 2014, **136**, 14570–14575.
17 J. Burschka, N. Pellet, S.-J. Moon, R. Humphry-Baker, P. Gao, M. K. Nazeeruddin and M. Grätzel, *Nature*, 2013, **499**, 316–319.
18 K. T. Butler, J. M. Frost and A. Walsh, *Mater. Horiz.*, 2015, **2**, 228–231.
19 S. Aharon, B. El Cohen and L. Etgar, *J. Phys. Chem. C*, 2014, **118**, 17160–17165.
20 J. Feng and B. Xiao, *J. Phys. Chem. Lett.*, 2014, **3**, 19655–19660.
21 S. Ryu, J. H. Noh, N. J. Jeon, Y. C. Kim, W. S. Yang, J. Seo and S. Il Seok, *Energy Environ. Sci.*, 2014, **7**, 2614–2618.
22 A. Abrusci, S. D. Stranks, P. Docampo, H.-L. Yip, A. K.-Y. Jen and H. J. Snaith, *Nano Lett.*, 2013, **13**, 3124–3128.
23 H. Azimi, T. Ameri, H. Zhang, Y. Hou, C. O. R. Quiroz, J. Min, M. Hu, Z.-G. Zhang, T. Przybilla, G. J. Matt, E. Spiecker, Y. Li and C. J. Brabec, *Adv. Energy Mater.*, 2015, **5**, 1401692.
24 L. Barnea-Nehoshtan, S. Kirmayer, E. Edri, G. Hodes and D. Cahen, *J. Phys. Chem. Lett.*, 2014, **5**, 2408–2413.
25 A. Barrows, A. Pearson, C. Kwak, A. Dunbar, A. Buckley and D. Lidzey, *Energy Environ. Sci.*, 2014, **7**, 2944–2950.
26 J. H. Noh, S. H. Im, J. H. Heo, T. N. Mandal and S. Il Seok, *Nano Lett.*, 2013, **13**, 1764–1769.
27 Y. Chen, Y. Zhao and Z. Liang, *Chem. Mater.*, 2015, **27**, 1448–1451.
28 Y.-S. Chen, J. S. Manser and P. V. Kamat, *J. Am. Chem. Soc.*, 2015, **137**, 974–981.
29 G. E. Eperon, V. M. Burlakov, P. Docampo, A. Goriely and H. J. Snaith, *Adv. Funct. Mater.*, 2014, **24**, 151–157.
30 M. Yang, Y. Zhou, Y. Zeng, C.-S. Jiang, N. P. Padture and K. Zhu, *Adv. Mater.*, 2015, **27**, 6363–6370.
31 B. Yang, O. Dyck, J. Poplawsky, J. Keum, A. Puretzky, S. Das, I. N. Ivanov, C. M. Rouleau, G. Duscher, D. B. Geohegan and K. Xiao, *J. Am. Chem. Soc.*, 2015, **137**, 9210–9213.
32 M. Saliba, T. Matsui, J.-Y. Seo, K. Domanski, N. Correa-Baena, K. Juan-Pablo Mohammad, S. M. Zakeeruddin, W. Tress, A. Abate, A. Hagfeldt and M. Gratzel, *Energy Environ. Sci.*, 2016, 1989–1997.
33 D. Liu and T. L. Kelly, *Nat. Photonics*, 2013, **8**, 133–138.
34 J. Huang, K. Jiang, X. Cui, Q. Zhang, M. Gao, M. Su, L. Yang and Y. Song, *Sci. Rep.*, 2015, **5**, 15889.
35 K. Hwang, Y. S. Jung, Y. J. Heo, F. H. Scholes, S. E. Watkins, J. Subbiah, D. J. Jones, D. Y. Kim and D. Vak, *Adv. Mater.*, 2015, **27**, 1241–1247.
36 J. M. Ball, M. M. Lee, A. Hey and H. J. Snaith, *Energy Environ. Sci.*, 2013, **6**, 1739–1743.
37 P. Docampo, J. M. Ball, M. Darwich, G. E. Eperon and H. J. Snaith, *Nat. Commun.*, 2013, **4**, 2761.
38 M. M. Tavakoli, K.-H. Tsui, Q. Zhang, J. He, Y. Yao, D. Li, Z. Fan, S.-F. Leung, Q. Zhang, J. He, Y. Yao, D. Li and Z. Fan, *ACS Nano*, 2015, **9**, 10287–10295.
39 M. Kaltenbrunner, G. Adam, E. D. Głowacki, M. Drack, R. Schwödiauer, L. Leonat, D. H. Apaydin, H. Groiss, M. C. Scharber, M. S. White, N. S. Sariciftci and S. Bauer, *Nat. Mater.*, 2015, **14**, 1032–1039.
40 Y.-F. Chiang, J.-Y. Jeng, M.-H. Lee, S.-R. Peng, P. Chen, T.-F. Guo, T.-C. Wen, Y.-J. Hsu and C.-M. Hsu, *Phys. Chem. Chem. Phys.*, 2014, **16**, 6033–6040.
41 Y. Han, S. Meyer, Y. Dkhissi, K. Weber, J. M. Pringle, U. Bach, L. Spiccia and Y.-B. Cheng, *J. Mater. Chem. A*, 2015, **3**, 8139–8147.
42 S. Aharon, S. Gamliel, B. El Cohen and L. Etgar, *Phys. Chem. Chem. Phys.*, 2014, **16**, 10512–10518.

43 F. Hao, C. C. Stoumpos, Z. Liu, R. P. H. Chang and M. G. Kanatzidis, *J. Am. Chem. Soc.*, 2014, **136**, 16411–16419.
44 B. A. Nejand, V. Ahmadi and H. R. Shahverdi, *ACS Appl. Mater. Interfaces*, 2015, **7**, 21807–21818.
45 X. Xu, Z. Liu, Z. Zuo, M. Zhang, Z. Zhao, Y. Shen, H. Zhou, Q. Chen, Y. Yang and M. Wang, *Nano Lett.*, 2015, **15**, 2402–2408.
46 K. Cao, Z. Zuo, J. Cui, Y. Shen, T. Moehl, S. M. Zakeeruddin, M. Grätzel and M. Wang, *Nano Energy*, 2015, **17**, 171–179.
47 Z. Liu, M. Zhang, X. Xu, L. Bu, W. Zhang, W. Li, Z. Zhao, M. Wang, Y.-B. Cheng and H. He, *Dalton Trans.*, 2015, **44**, 3967–3973.
48 S. K. Sarkar, A. S. Subbiah, A. Halder, S. Ghosh, N. Mahuli and G. Hodes, *J. Phys. Chem. Lett.*, 2014, **5**, 1748–1753.
49 J. Jeng, K. Chen, T. Chiang, P. Lin, T. Tsai, Y. Chang, T. Guo, P. Chen, T. Wen and Y. Hsu, *Adv. Mater.*, 2014, **26**, 4107–4113.
50 J. H. Kim, P. Liang, S. T. Williams, N. Cho, C. Chueh, M. S. Glaz, D. S. Ginger and A. K. Jen, *Adv. Mater.*, 2015, **27**, 695–701.
51 P. Qin, S. Tanaka, S. Ito, N. Tetreault, K. Manabe, H. Nishino, M. K. Nazeeruddin and M. Gra, *Nat. Nanotechnol.*, 2014, **5**, 3834.
52 P. Qin, M. Paulose, M. I. Dar, T. Moehl, N. Arora, P. Gao, O. K. Varghese, M. Grätzel and M. K. Nazeeruddin, *Small*, 2015, **11**, 5533–5539.
53 Z.-L. Tseng, C.-H. Chiang and C.-G. Wu, *Sci. Rep.*, 2015, **5**, 13211.
54 T. Liu, L. Liu, M. Hu, Y. Yang, L. Zhang, A. Mei and H. Han, *J. Power Sources*, 2015, **293**, 533–538.
55 F. Zhang, X. Yang, H. Wang, M. Cheng, J. Zhao and L. Sun, *ACS Appl. Mater. Interfaces*, 2014, **6**, 16140–16146.
56 Z. Li, S. A. Kulkarni, P. P. Boix, E. Shi, A. Cao, K. Fu, S. K. Batabyal, J. Zhang, Q. Xiong, L. H. Wong, N. Mathews and S. G. Mhaisalkar, *ACS Nano*, 2014, **8**, 6797–6804.
57 C.-Y. Chan, Y. Wang, W. Guan-Wei and E. W.-G. Diau, *J. Mater. Chem.*, 2016, **4**, 3872–3878.
58 L. Zonghao, Z. Meng, X. Xiaobao, C. Fensha, Y. Huailiang, B. Lingling, L. Wenhui, Z. Aili, Z. Zhixin, W. Mingkui, C. Yi-Bing and H. He, *J. Mater. Chem. A*, 2015, **3**, 24121–24127.
59 W. S. Yang, J. H. Noh, N. J. Jeon, Y. C. Kim, S. Ryu, J. Seo and S. Il Seok, *Science*, 2015, **348**, 1234–1237.
60 J. H. Kim, S. T. Williams, N. Cho, C. Chueh and A. K. Jen, *Adv. Energy Mater.*, 2015, **5**, 1401229.
61 K. Hwang, Y. Jung, Y. Heo, F. H. Scholes, S. E. Watkins, J. Subbiah, D. J. Jones, D. Kim and D. Vak, *Adv. Mater.*, 2015, **27**, 1241–1247.
62 Q. Lin, A. Armin, R. Chandra, R. Nagiri, P. L. Burn and P. Meredith, *Nat. Photonics*, 2015, **9**, 106–112.
63 Y. Li, L. Meng, Y. M. Yang, G. Xu, Z. Hong, Q. Chen, J. You, G. Li, Y. Yang and Y. Li, *Nat. Commun.*, 2016, **7**, 10214.
64 D. Liu and T. L. Kelly, *Nat. Photonics*, 2014, **8**, 133–138.
65 S. Sun, T. Salim, N. Mathews, M. Duchamp, C. Boothroyd, G. Xing, T. C. Sum and Y. M. Lam, *Energy Environ. Sci.*, 2014, **7**, 399–407.
66 T. Leijtens, G. E. Eperon, S. Pathak, A. Abate, M. M. Lee and H. J. Snaith, *Nat. Commun.*, 2013, **4**, 2885.
67 Y. Kato, L. K. Ono, M. V. Lee, S. Wang, S. R. Raga and Y. Qi, *Adv. Mater. Interfaces*, 2015, **2**, 1500195.
68 X. Zhou, C. Bao, F. Li, H. Gao, T. Yu, J. Yang, W. Zhu and Z. Zou, *RSC Adv.*, 2015, **5**, 58543–58548.
69 I. Jeong, H. J. Kim, B. Lee, H. J. Son, J. Y. Kim, D. Lee, D. Kim, J. Lee, M. J. Ko, I. Jeong, H. J. Kim, B. Lee, H. J. Son, J. Y. Kim, D. Lee, D. Kim, J. Lee and M. J. Ko, *Nano Energy*, 2015, **17**, 131–139.
70 Q. Jiang, X. Sheng, B. Shi, X. Feng and T. Xu, *J. Phys. Chem. B*, 2014, **118**, 25878–25883.
71 D. Bryant, P. Greenwood, J. Troughton, M. Wijdekop, M. Carnie, M. Davies, K. Wojciechowski, H. Snaith, T. Watson and D. Worsley, *Adv. Mater.*, 2014, 7499–7504.
72 J. M. Foster, H. J. Snaith, T. Leijtens and G. Richardson, *SIAM J. Appl. Math.*, 2014, **74**, 1935–1966.
73 L. Etgar, P. Gao, Z. Xue, Q. Peng, A. K. Chandiran, B. Liu, M. K. Nazeeruddin and M. Grätzel, *J. Am. Chem. Soc.*, 2012, **134**, 17396–17399.
74 X. Liu, C. C. Wang, L. Lyu, C. C. Wang, Z. Xiao, C. Bi, J. Huang and Y. Gao, *Phys. Chem. Chem. Phys.*, 2014, **17**, 896–902.
75 H. B. Michaelson, *J. Appl. Phys.*, 1977, **48**, 4729–4733.
76 Y. S. Lim, J. Jeong, J. Y. Kim, M. J. Ko, H. Kim, B. Kim, U. Jeong and D. K. Lee, *J. Phys. Chem. C*, 2013, **117**, 11930–11940.
77 H. J. Snaith, *J. Phys. Chem. Lett.*, 2013, **4**, 3623–3630.
78 J. H. Heo, S. H. Im, J. H. Noh, T. N. Mandal, C.-S. Lim, J. A. Chang, Y. H. Lee, H. Kim, A. Sarkar, M. K. Nazeeruddin, M. Grätzel and S. Il Seok, *Nat. Photonics*, 2013, **7**, 486–491.
79 E. M. Miller, Y. Zhao, C. C. Mercado, S. K. Saha, J. M. Luther, K. Zhu, V. Stevanović, C. L. Perkins and J. van de Lagemaat, *Phys. Chem. Chem. Phys.*, 2014, **16**, 22122–22130.
80 W. A. Laban and L. Etgar, *Energy Environ. Sci.*, 2013, **6**, 3249–3253.
81 S. Gamliel, A. Dymshits, S. Aharon, E. Terkieltaub and L. Etgar, *J. Phys. Chem. C*, 2015, **119**, 19722–19728.
82 A. Dymshits, A. Rotem and L. Etgar, *J. Mater. Chem. A*, 2014, **2**, 20776–20781.
83 W. Yin, T. Shi and Y. Yan, *Appl. Phys. Lett.*, 2014, **104**, 063903.
84 K. Miyano, N. Tripathi, M. Yanagida and Y. Shirai, *Acc. Chem. Res.*, 2016, 303–310.
85 A. Walsh, D. O. Scanlon, S. Chen, X. G. Gong and S. Wei, *Angew. Chem., Int. Ed.*, 2015, 1791–1794.
86 A. Dymshits, A. Henning, G. Segev, Y. Rosenwaks and L. Etgar, *Sci. Rep.*, 2015, **5**, 8704.
87 K.-G. Lim, S. Ahn, Y.-H. Kim, Y. Qi and T.-W. Lee, *Energy Environ. Sci.*, 2016, **9**, 932–939.
88 C. Quarti, E. Mosconi and F. De Angelis, *Chem. Mater.*, 2014, **26**, 6557–6569.
89 F. Behrouznejad and N. Taghavinia, *ChemElectroChem*, 2014, **1**, 944–950.
90 F. Behrouznejad and N. Taghavinia, *J. Power Sources*, 2014, **260**, 299–306.

91 F. Behrouznejad, N. Taghavinia, M. Pazoki and F. Tajabadi, *Phys. Chem. Chem. Phys.*, 2016, **18**, 5244–5252.
92 E. Guillén, F. J. Ramos, J. A. Anta and S. Ahmad, *J. Mater. Chem. C*, 2014, **118**, 22913–22922.
93 R. S. Sanchez, V. Gonzalez-Pedro, J. W. Lee, N. G. Park, Y. S. Kang, I. Mora-sero and J. Bisquert, *J. Phys. Chem. Lett.*, 2014, **5**, 2357–2363.
94 C. S. Shim and C. K. Hong, *NPG Asia Materials*, 2015, **7**, e208.
95 C. Eames, J. M. Frost, P. R. F. Barnes, B. C. O'Regan, A. Walsh and M. S. Islam, *Nat. Commun.*, 2015, **6**, 7497.
96 J. M. Azpiroz, E. Mosconi, J. Bisquert and F. De Angelis, *Energy Environ. Sci.*, 2015, **8**, 2118–2127.
97 B. Chen, Y. Deng, H. Tong and J. Ma, *Superlattices Microstruct.*, 2014, **69**, 194–203.
98 J. I. Gersten and F. W. Smith, *The Physics and Chemistry of Materials*, Wiley, 2001.
99 N. E. Christensen and B. O. Seraphin, *Phys. Rev. B: Solid State*, 1971, **4**, 3321–3344.
100 N. E. Christensen, *Int. J. Quantum Chem.*, 1984, **25**, 233–261.
101 C. M. Lewandowski, *Gold, science and applications*, 2015, vol. 1.
102 H. Schmidbaur, S. Cronje, B. Djordjevic and O. Schuster, *Chem. Phys.*, 2005, **311**, 151–161.
103 M. Jansen, *Solid State Sci.*, 2005, **7**, 1464–1474.
104 P. Pyykko and J. P. Desclaux, *Acc. Chem. Res.*, 1979, **12**, 276–281.